American Mineralogist, Volume 95, pages 1657–1670, 2010

XRD, micro-XANES, EMPA, and SIMS investigation on phlogopite single crystals from Mt. Vulture (Italy)

F. SCORDARI,[1,*] M.D. DYAR,[2] E. SCHINGARO,[1] M. LACALAMITA,[1] AND L. OTTOLINI[3]

[1]Dipartimento Geomineralogico, Università degli Studi di Bari, Via E. Orabona 4, I-70125 Bari, Italy
[2]Department of Astronomy, Mount Holyoke College, South Hadley, Massachusetts 01075, U.S.A.
[3]CNR-Istituto di Geoscienze e Georisorse (IGG), Sezione di Pavia, Via A. Ferrata, 1, I-27100 Pavia, Italy

ABSTRACT

Selected phlogopite flakes from Mt. Vulture in southern Italy were studied using a combination of single-crystal techniques: electron microprobe analysis (EMPA), secondary ion mass spectrometry (SIMS), single-crystal X-ray diffraction (SCXRD), and micro-X-ray absorption near-edge spectroscopy (XANES). The latter technique was employed to analyze the structure of the Fe-*K* absorption edge over the region from 7080–8100 eV and to determine $Fe^{3+}/\Sigma Fe$ at a micrometer scale, albeit with large error bars due to known effects of orientation on pre-edge energy.

The annite component, Fe/(Mg+Fe), of the samples studied ranged from 0.16 to 0.31, the Ti content from 0.11 to 0.27 atoms per formula unit (apfu) and the Ba content from 0.03 to 0.09 apfu. SIMS analysis showed H_2O (wt%) = 1.81–3.30, F (wt%) = 0.44–1.29, and Li_2O (wt%) = 0.001–0.027. The intra single-crystal chemical variability for major/minor elements (Mg, Fe, Al, Ba, Ti, and K) was found particularly significant for samples VUT191_11 and PG5_1, less significant for the other samples of the set. SIMS data relative to crystals VUT187_24, VUT191_10, VUT191_11, and VUT187_28 showed a noteworthy variation in the concentrations of some light elements (H, Li, and F) with coefficient of variation CV (as 1σ%) up to ~18% for H_2O.

The analyzed micas belong to the 1*M* polytype. Structure refinements using anisotropic displacement parameters were performed in space group *C*2/*m* and converged at $3.08 \leq R \leq 3.63$, $3.32 \leq R_w \leq 3.98\%$. Micro-XANES results yielded $Fe^{3+}/\Sigma Fe$ from 51–93%. Previous Mössbauer data from powdered samples suggested $Fe^{3+}/\Sigma Fe$ values ranging from 49–87%. However, the Fe^{3+} content determined by both techniques is sometimes remarkably different, in part because of the large errors (±10–15%) presently associated with the micro-XANES technique and in part because the Fe^{3+} content of a single crystal may significantly depart from the average value obtained from routine Mössbauer analysis.

The combination of EMPA, SIMS, and micro-XANES resulted in the characterization of the samples at a comparable spatial scale. By means of in-situ data and the results of crystallographic investigations, the occurrence of different relative amounts of M^{3+}-oxy $[{}^{VI}M^{2+} + (OH)^- \leftrightarrow {}^{VI}M^{3+} + O^{2-} + \frac{1}{2}H_2\uparrow]$, Ti-oxy substitutions $[{}^{VI}M^{2+} + 2(OH)^- \leftrightarrow {}^{VI}Ti^{4+} + 2O^{2-} + H_2\uparrow]$, and Ti-vacancy ($\square$) substitution $(2{}^{VI}M^{2+} \leftrightarrow {}^{VI}Ti^{4+} + {}^{VI}\square)$ was ascertained for the studied samples.

Keywords: Volcanic phlogopite, micro-XANES, SIMS, crystal chemistry, substitution mechanisms

INTRODUCTION

Historically, accurate knowledge of cation and anion populations in natural mica solid solutions has been hampered by the lack of complete chemical analyses. More recently, the determination of $Fe^{3+}/\Sigma Fe$ by Mössbauer spectroscopy on bulk samples has become routine, though chemical characterization of the anion site (i.e., quantitative evaluations of OH^-, O^{2-}, Cl^-, and F^-) is much less common. Such complete chemical characterization combined with structural analysis is needed to evaluate the extensive chemical disorder that affects cation sites of micas, because homo- and heterovalent substitutions occur at interlayer (K, Ba, Ca, Na, NH_4^+, H_2O, H_3O^+, $\square$, where $\square$ stands for vacancy), octahedral (Mg, Mn, Fe^{2+}, Fe^{3+}, $Ti^{3+,4+}$, Al, Cr, Li, $\square$), and tetrahedral (Si, Al, Fe, Ti) sites. This complicates assessment of the substitution mechanisms in micas, particularly in cases when multiple valence states and multiple substitutions may occur. As an example, Ti can be incorporated into the mica structure via: (1) cation substitution at the octahedral site with formation of vacancies, $2{}^{VI}M^{2+} \leftrightarrow {}^{VI}Ti^{4+} + {}^{VI}\square$, where M stands for Mg, Fe^{2+}, and Mn^{2+}. This is also known as the Ti-vacancy mechanism (Forbes and Flower 1974); (2) cation substitution at the octahedral site accompanied by the loss of protons at the anion site, ${}^{VI}M^{2+} + 2(OH)^- \leftrightarrow {}^{VI}Ti^{4+} + 2O^{2-} + H_2$, the Ti-oxy mechanism (Bohlen et al. 1980); and/or (3) a coupled octahedral-tetrahedral cation substitution, ${}^{VI}M^{2+} + 2{}^{IV}Si^{4+} \leftrightarrow {}^{VI}Ti^{4+} + 2{}^{IV}Al^{3+}$, the Ti-Tschermak substitution (Robert 1976). A combination of the above mechanisms may also occur, as well as other, rarer substitutions (Waters and Charnley 2002). Very recently, substantial Ti-oxy and Ti-vacancy substitutions have been found by Sassi et al. (2008) in biotite from high-grade metapelitic xenoliths, whereas Cesare et al. (2008) found that Ti may be also involved in a "fluorination" mechanism, $Ti^{4+} + 2O^{2-} \leftrightarrow (Fe, Mg)^{2+} + 2F^-$. Different authors have ascertained that Fe^{3+}-oxy substitutions

---

[*] E-mail: f.scordari@geomin.uniba.it

0003-004X/10/1112–1657$05.00/DOI: 10.2138/am.2010.3442

$[^{VI}M^{2+} + (OH)^- \leftrightarrow {}^{VI}Fe^{3+} + O^{2-} + ½H_2]$ other than Ti-oxy substitutions may play a major role both in metamorphic and igneous phlogopites (Virgo and Popp 2000; Righter et al. 2002; Cesare et al. 2003; Ventruti et al. 2008).

The special interest in the biotite composition is due to its potential use in geothermometry and geobarometry, where $Fe^{3+}/\Sigma Fe$, hydroxyl, and Ti concentrations can be used to evaluate magmatic f_{O_2}, f_{H_2O}, temperatures of formation, etc. (Henry and Guidotti 2002; Cesare et al. 2003, 2008; Henry et al. 2005). For igneous micas, the use of biotite composition as a tectonomagmatic indicator has also been suggested (Shabani et al. 2003, and references therein). However, it is widely acknowledged that the crystal chemistry of volcanic micas represents a challenge, because its variation depend on the evolution of the micas host rocks. The latter very often were subjected to complex geological evolution, with occurrence of non equilibrium conditions, so that multiple mica populations, intergranular and intragranular variability, etc., further complicate the task of mica characterization and the development of activity compositions models from which magmatic intensive variables can be determined (Feldstein et al. 1996; Waters and Charnley 2002; Brigatti et al. 2005; Scordari et al. 2006; Matarrese et al. 2008). Only recently, Fabbrizio et al. (2006, 2009) have shown that biotite may be used to estimate water fugacity (f_{H_2O}) in any magmatic system in which biotite-magnetite-sanidine is a stable assemblage. However, those authors point out that the complexity of biotite solid solutions constitutes a major obstacle to the use of this geohygrometer. Indeed, the choice of a proper annite activity model depends on a full understanding of substitution mechanisms in biotite.

To obtain a better understanding of volcanic mica crystal chemistry, electron microprobe analysis (EMPA), Mössbauer spectroscopy, manometry, and secondary ion mass spectrometry (SIMS) have been used (Dyar et al. 1991, 1993; Feldstein et al. 1996; Virgo and Popp 2000; Righter et al. 2002; see also review in Dyar 2002). However, details about substitution mechanism in micas can be obtained only if such studies also include cation site occupancies, locations, and site geometries from a structure refinement (e.g., Cesare et al. 2003, 2008; Brigatti et al. 2005; Scordari et al. 2006; Matarrese 2007; Schingaro et al. 2007; Matarrese et al. 2008; Sassi et al. 2008; Lacalamita 2009). These papers combine single-crystal techniques, i.e., EMPA, SIMS, single-crystal X-ray diffraction (SCXRD) with powder techniques, i.e., Mössbauer spectroscopy, C-H-N elemental analysis, etc.

In the present work, a suite of phlogopites from Mt. Vulture (southern Italy), selected also on the basis of previously reported grain to grain variation of micas even from the same rock sample (Matarrese et al. 2008), has been studied using a combination of the following single-crystal techniques: EMPA, SEM, SIMS, SCXRD, and micro-scale X-ray absorption near-edge spectroscopy (XANES). Out of these, EMPA, SIMS, and micro-XANES allow the characterization of samples at a comparable spatial scale. The integration of the results coming from the selected techniques is expected to provide further insights into the complex substitution mechanisms characteristic of micas.

MATERIALS AND EXPERIMENTAL METHODS

The explosive-effusive volcanic activity at Mt. Vulture lasted about 750 ka and produced a large variety of alkaline, SiO_2-undersaturated volcanic rocks ranging from carbonatites and melilitites, to foidites, phonolitic-foidites, tephritic-phonolites, and phonolites (Stoppa et al. 2006). The rocks are classified on the basis of their age (Buettner et al. 2006) as old (~700 ka), intermediate (~600–550 ka), and young (~130 ka). Details on the classification of the Vulture deposits are published elsewhere (Matarrese 2007; Schingaro et al. 2007; Matarrese et al. 2008). In the present work, seven single crystals have been considered, out of which one (labeled PG5_1) is from the old deposits, five (VUT187_13, VUT187_24, VUT187_28, VUT191_10, and VUT 191_11) are from intermediate deposits, and one (VUT0001_2) is from the most recent deposits. The crystals size ranged from 0.2–0.3 mm to several millimeters. These samples were selected from a larger suite of micas from the Vulture sequence (Matarrese 2007) for which Mössbauer spectra on powders have been already measured (Schingaro et al. 2007; Matarrese et al. 2008; and unpublished data). Specifically, the five single crystals from intermediate deposits have already been investigated by EMPA and SCXRD in previous works (Schingaro et al. 2007; Matarrese et al. 2008) but they needed extra investigation because they exhibited grain-to-grain variation and the characterization of the light elements was missing. In the present work, the relevant chemical analytical data are completed and the crystal-chemical formulas revised on the light of SIMS and micro-XANES results.

EMPA

Major elements compositions were determined on seven single crystals embedded in epoxy resin. The compositions of samples VUT0001_2 and PG5_1 have been determined for the first time, whereas partial analytical data were available for samples VUT187_13, VUT187_24, VUT187_28, VUT191_10, and VUT 191_11 from previous studies (Schingaro et al. 2007; Matarrese et al. 2008) and comprehensive analytical data are completed in this study. The compositions were measured using a Cameca SX-50 electron microprobe at the Istituto di Geologia Ambientale e Geoingegneria, CNR, Rome, with the following operating conditions: 15 kV accelerating voltage, 15 nA specimen beam current, and 10 μm beam diameter, WD spectrometers. The following standards were employed: jadeite (Na), periclase (Mg), wollastonite (Si and Ca), rutile (Ti), corundum (Al), magnetite (Fe), orthoclase (K), barite (Ba), fluor-phlogopite (F), and sylvite (Cl). A conversion from X-ray counts to oxide weight percentages (wt%) was obtained with the PAP procedure (Pouchou and Pichoir 1985). The measurements are affected by a relative analytical uncertainty of 1% for major elements and 4% for minor elements.

SIMS

SIMS measurements were performed on seven single crystals with a CAMECA IMS 4f ion microprobe installed at CNR-IGG, Pavia (Italy). A –12.5 kV accelerated $^{16}O^-$ primary-ion beam was used with a current intensity of 3–7 nA and <5–10 μm beam diameter, following procedures similar to those adopted by Luisa Ottolini in the paper by Mesto et al. (2006). Each sample was mounted with standards and left to degas overnight in the ion-microprobe sample chamber. Secondary-ion signals of the following isotopes were monitored at the electron multiplier: $^1H^+$, $^7Li^+$, $^{19}F^+$, and $^{30}Si^+$ (the latter was used as the inner reference for the matrix). Acquisition times were 20 s (H), 10 s (Li), 50 s (F), and 15 s (Si) over five analytical cycles. Positive secondary ions in the range of 75–125 eV emission kinetic energies were detected under steady-state sputtering conditions after 15 min of pre-sputtering. According to previous SIMS work on light elements in silicates, the analysis of "filtered" secondary ions is useful in reducing most chemical matrix effects and in improving the overall measurement reproducibility (Ottolini et al. 1993, 1995, and references therein). Several medium-silica silicate standards were employed for the quantification of the ion signals for H, Li, and F: Finero phlogopite (SiO_2 = 40.04 wt%, 4.20 wt% H_2O, 712 ppm F), kornerupine no. 6, schorl no. 16, dravite no. 18, and elbaite no. 19 (Ottolini et al. 2002). In particular, we adopted empirical corrections to the IY(H/Si) to consider the variation of the ion signals with increasing (Fe+Mn+Ti) content in the sample, as fully described in Ottolini and Hawthorne (2001), Ottolini et al. (2002), and Kogarko et al. (2005). The sample mounts were then re-polished smoothly, carbon-coated, and analyzed again on the electron microprobe at spots proximal to the SIMS craters. These EMPA data were then used in the final SIMS quantification procedures.

SEM

Backscattered electron (BSE) images were acquired at the Dipartimento Geomineralogico, Università di Bari, with an EVO50XVP LEO scanning electron microscope (SEM) coupled with an Oxford-Link Ge ISIS energy dispersive spectrometer. Operating conditions were: 15 kV accelerating voltage, probe current 500 nA, working distance 17–20 mm.

X-ray maps

X-ray elemental maps were obtained with a JEOL JXA-8200 electron microprobe (WDS mode), installed at the Dipartimento di Scienze della Terra, Università di Milano. The analytical conditions were accelerating voltage 15 kV; probe current 5 nA, probe diameter <1 μm, and dwell time 40 ms.

Micro-XANES

Micro-XANES analyses for Fe^{3+} were performed on the seven single crystals as employed for SIMS analysis using the structure of the Fe *K* absorption edge scanned in the pre-edge region. Incident beam energies from 50 eV below the main absorption edge energy (about 7111 eV for Fe) to about 60 eV above the main edge were used. The measured Fe *K* fluorescence line intensities were normalized to the ion chamber current and corrected for dead-time.

Measurements were made using the synchrotron X-ray fluorescence microprobe at the National Synchrotron Light Source (NSLS), Brookhaven, New York (beam line X26A), following the methods described in Bajt et al. (1994) and Delaney et al. (1996). The synchrotron beam passes through a Si(311) monochromator, focusing mirror, and a beam-defining aperture to produce an incident beam of about 8 × 10 μm on the sample. The Si (Li) detector was mounted at 90° to the incident beam. Only Fe-XANES data were collected, because the other major elements (with invariant valence states) are well characterized by EMPA. Energy intervals were 0.3 eV over the energy range closest to the main absorption edge energy (–10 to +20 eV) and 2 eV intervals for the remaining energy ranges. Each energy increment was measured for between 3 and 10 live seconds, dependent on the Fe content of the sample. In the adopted experimental setup, the beam impinges at a 45° angle to the surface of the mineral grain. The mica samples were not oriented prior to the measurement. However, two spectra were recorded from two close spots on each individual grain, hereafter indicated as A and B, with different orientations relative to the fixed beam polarization direction; these were obtained by simply rotating the sample by a random amount to change the orientation of the crystal relative to the beam polarization.

The pre-edge peak envelope was measured relative to a calibration line based on randomly oriented magnetite, hematite, fayalite, and acmite single crystals that were analyzed throughout a single injection (following Bajt et al. 1994). To correct for monochromator drift, magnetite was typically analyzed every fourth analysis, and spectra were individually corrected to "true" energies using an offset based on the known position of the magnetite peak centroid at 7113.25 eV (see Petit et al. 2001; Wilke et al. 2001).

SCXRD

X-ray diffraction analysis of two selected single crystals (VUT0001_2 and PG5_1) was performed using a Bruker AXS X8 APEX II CCD automated diffractometer equipped with a four-circle Kappa goniometer and graphite monochromatized Mo$K\alpha$ radiation. The relevant data for the remaining five crystals here considered are reported elsewhere (Schingaro et al. 2007; Matarrese et al. 2008).

A set of 36 frames was used for initial cell determination, with a crystal-to-detector distance of 40 mm and a strategy optimized by the Apex suite program (Bruker 2003a). Complete data collection was then accomplished by several φ and ω scans with 0.5° rotation and 10 s exposure time per frame. The whole Ewald sphere $(\pm h, \pm k, \pm l)$ was recorded in theta ranges up to ~40°. Reflection intensities were extracted and corrected for Lorentz-polarization using the SAINT program (Bruker 2003b). Absorption correction was applied using SADABS (Sheldrick 2003). Least-squares refinement were performed using the program CRYSTALS (Betteridge et al. 2003) in the space group $C2/m$. Starting atomic coordinates were taken from Mesto et al. (2006). The refined parameters were scale factors, atomic positions, cation occupancy factors, and anisotropic displacement parameters. Details on the refinement strategy are reported in Matarrese et al. (2008).

RESULTS

Chemical analyses

EMPA results representing averages over 5–12 spots per crystal are given in terms of oxide wt% in Table 1. Table 2 contains the atomic proportions [atoms per formula units (apfu)] calculated from Table 1 on the basis of 12 (O, OH$^-$, F, Cl), assuming all Ti is Ti^{4+} and using the Fe^{2+}/Fe^{3+} ratios provided from micro-XANES investigation (see below).

For some of the major and minor elements, a significant amount of chemical variability exists among the samples: MgO 14.72–20.90 wt%, FeO_{tot} 7.21–11.68 wt%, TiO_2 2.03–4.65 wt%, Na_2O 0.59–0.77 wt%, BaO 0.88–2.98 wt%. In general, the chemical variability within the crystals (i.e., intragranular variability) ranged from low (as in sample VUT187_13) to high (as in samples VUT191_11, PG5_1), as evidenced from the analysis of five crystals in Figures 1a–1e (available on deposit[1]),

TABLE 1. Average microprobe analyses (wt%)

Sample	VUT0001_2	VUT187_13*	VUT187_24*	VUT187_28*	VUT191_10†	VUT191_11†	PG5_1
no. spots	7	5	12	5	7	7	10
SiO_2	37.10(28)	35.83(20)	36.89(47)	36.35(30)	33.60(30)	33.98(62)	35.95(44)
Al_2O_3	17.37(25)	16.54(04)	16.11(21)	15.62(10)	15.88(14)	15.73(35)	16.68(27)
MgO	20.90(85)	19.68(05)	18.82(16)	19.45(18)	15.59(23)	14.72(46)	18.73(26)
FeO_{tot}	7.21(21)	8.71(14)	9.78(10)	7.78(14)	11.60(27)	11.68(22)	8.55(18)
TiO_2	2.24(05)	2.28(04)	2.94(04)	3.70(03)	4.62(15)	4.65(57)	2.03(07)
Cr_2O_3	0.01(02)	0.02(02)	0.02(02)	0.07(09)	0.01(01)	0.00(01)	0.01(01)
MnO	0.07(03)	0.05(03)	0.09(03)	0.07(06)	0.12(05)	0.18(01)	0.07(04)
NiO	0.00(03)	0.04(05)	0.02(02)	0.03(03)	0.02(02)	0.03(02)	0.03(02)
Li_2O‡	0.0045	0.00109(20)	0.0042(11)	0.0090(18)	0.0102(39)	0.0142(62)	0.027(15)
K_2O	8.74(17)	8.58(10)	8.84(09)	8.67(10)	8.09(16)	7.75(38)	8.85(17)
Na_2O	0.63(04)	0.73(04)	0.77(03)	0.67(10)	0.59(02)	0.60(08)	0.73(02)
BaO	0.92(06)	1.19(04)	1.03(07)	1.18(05)	2.40(37)	2.98(1.14)	0.88(06)
CaO	0.04(02)	0.02(02)	0.02(01)	0.02(03)	0.03(05)	0.08(07)	0.03(03)
F	0.93(07)	0.37(03)	0.35(13)	0.70(11)	0.62(14)	0.95(06)	0.49(09)
F‡	0.43	0.60(04)	0.50(03)	0.94(47)	0.95(02)	1.29(06)	0.54(04)
Cl	0.01(01)	0.01(01)	0.00(00)	0.02(02)	0.08(01)	0.09(03)	0.01(01)
H_2O‡	3.30	3.14(01)	3.02(55)	2.79(11)	2.30(33)	1.81(16)	3.05(17)
FeO§(A)	2.82	1.47	3.33	3.06	5.34	–	4.21
Fe_2O_3§(A)	4.88	8.13	7.17	5.25	6.96	–	4.83
FeO§(B)	0.51	–	1.86	3.36	5.75	4.29	4.15
Fe_2O_3§(B)	7.45	–	8.80	4.91	6.50	8.22	4.89

Notes: Standard deviations are given in parentheses.
* EMPA data from Schingaro et al. (2007).
† EMPA data from Matarrese et al. (2008).
‡ SIMS data.
§ XANES results used to recast FeO_{tot} into FeO and Fe_2O_3; A and B refer to different runs (see text).

---

[1] Deposit item AM-10-056, Figure 1 and CIFs. Deposit items are available two ways: For a paper copy contact the Business Office of the Mineralogical Society of America (see inside front cover of recent issue) for price information. For an electronic copy visit the MSA web site at http://www.minsocam.org, go to the *American Mineralogist* Contents, find the table of contents for the specific volume/issue wanted, and then click on the deposit link there.

Table 2. Atomic proportions (apfu) as determined by combining EMPA, XANES, and SIMS analyses for the samples given in Table 1

	VUT0001_2	VUT187_13*‡	VUT187_24*	VUT187_28*	VUT191_10†	VUT191_11†‡	PG5_1
				XANES (Run A)			
Si	2.688	2.650	2.709	2.710	2.623	2.668	2.709
^{IV}Al	1.312	1.350	1.291	1.290	1.377	1.332	1.291
ΣTet.	4.000	4.000	4.000	4.000	4.000	4.000	4.000
^{VI}Al	0.172	0.092	0.103	0.083	0.083	0.124	0.191
Mg	2.258	2.170	2.060	2.162	1.814	1.723	2.104
Fe^{2+}	0.171	0.091	0.204	0.191	0.348	0.282	0.264
Fe^{3+}	0.266	0.452	0.396	0.294	0.409	0.486	0.275
Ti	0.122	0.127	0.162	0.207	0.271	0.275	0.115
Cr	0.001	0.003	0.003	0.009	0.001	0.000	0.001
Mn	0.004	0.003	0.005	0.004	0.008	0.012	0.004
Ni	0.000	0.002	0.001	0.002	0.001	0.002	0.002
Li	0.001	0.001	0.001	0.003	0.003	0.045	0.008
ΣOct.	2.995	2.938	2.935	2.953	2.938	2.946	2.962
Vacancy	0.005	0.062	0.065	0.047	0.062	0.054	0.038
K	0.808	0.809	0.828	0.825	0.805	0.776	0.851
Na	0.089	0.104	0.109	0.097	0.090	0.091	0.107
Ba	0.026	0.034	0.030	0.034	0.073	0.092	0.026
Ca	0.000	0.002	0.001	0.002	0.002	0.006	0.002
ΣInt.	0.923	0.950	0.968	0.957	0.971	0.965	0.986
OH	1.596	1.550	1.481	1.384	1.199	0.949	1.535
OH*	1.52	1.28	1.30	1.08	1.01	0.92	1.53
F	0.099	0.140	0.117	0.222	0.235	0.320	0.129
Cl	0.001	0.001	0.000	0.002	0.011	0.012	0.001
				XANES (Run B)			
Si	2.672	–	2.698	2.712	2.626	–	2.709
^{IV}Al	1.328	–	1.302	1.288	1.374	–	1.291
ΣTet.	4.000	–	4.000	4.000	4.000	–	4.000
^{VI}Al	0.146	–	0.088	0.086	0.088	–	0.190
Mg	2.244	–	2.052	2.163	1.816	–	2.103
Fe^{2+}	0.030	–	0.114	0.210	0.376	–	0.261
Fe^{3+}	0.400	–	0.485	0.276	0.382	–	0.278
Ti	0.121	–	0.162	0.208	0.272	–	0.115
Cr	0.001	–	0.003	0.009	0.001	–	0.001
Mn	0.004	–	0.005	0.004	0.008	–	0.004
Ni	0.002	–	0.001	0.002	0.001	–	0.002
Li	0.001	–	0.001	0.003	0.003	–	0.008
ΣOct.	2.952	–	2.909	2.958	2.946	–	2.961
Vacancy	0.048	–	0.091	0.042	0.054	–	0.039
K	0.803	–	0.825	0.825	0.806	–	0.851
Na	0.089	–	0.109	0.097	0.090	–	0.107
Ba	0.026	–	0.030	0.034	0.073	–	0.026
Ca	0.002	–	0.001	0.002	0.002	–	0.002
ΣInt.	0.919	–	0.965	0.958	0.972	–	0.986
OH	1.587	–	1.475	1.385	1.200	–	1.534
OH§	1.52	–	1.30	1.08	1.01	–	1.53
F	0.098	–	0.117	0.222	0.235	–	0.129
Cl	0.001	–	0.000	0.002	0.011	–	0.001

Note: Tet. = Tetrahedral; Oct. = Octahedral; Int. = Interlayer.

* EMPA data from Schingaro et al. (2007).

† EMPA data from Matarrese et al. (2008).

‡ Where XANES data were not available, the atomic proportion was not calculated.

§ OH groups evaluated from the *c*-parameter from the equation: $c = 10.065(16) + 0.125(13)\text{OH}$ (Ventruti et al. 2008).

where the results of a second session of EMP analyses (traverses from rim to rim) are reported. SEM-BSE images, obtained from the two samples VUT191_11 and VUT187_13, show that VUT191_11 has variable composition on a micrometer scale. Figure 2a illustrates chemical zoning on crystal VUT191_11 used both for electron and SIMS analysis. The sample surface shows three distinct styles of growth zoning: internal chaotic growth zoning, oscillatory zoning, and homogeneous growth after a period of partial resorption. The SIMS analyses, whose distinctive craters after ion bombardment are visible as holes in Figure 2a, were done mainly in the internal zone of the crystal. Figure 2b shows a SEM-BSE image of the same sample after surface re-polishing by several micrometers to check for in depth variability. Note that the contrast due to the chemical zoning is slightly reduced in the internal zone but apatite crystal inclusions are now evident. From the inspection of Figure 2c and 2d, it is apparent that sample VUT187_13 is, instead, homogeneous. From Figure 2e, it can be argued that the brighter regions visible in Figures 2a and 2b are related to enrichment in Ba and Ti with respect to K and Mg.

For light elements, the single spots from SIMS analysis are reported on Table 3. The number of SIMS spots per sample was strictly dependent on the dimensions of the grain. Indeed due to the tiny crystal size, further reduced in some case by re-polishing the sample mount, the SIMS spots varied from 2 (VUT187_28) to 5 (VUT191_10 and VUT191_11), with the exception of

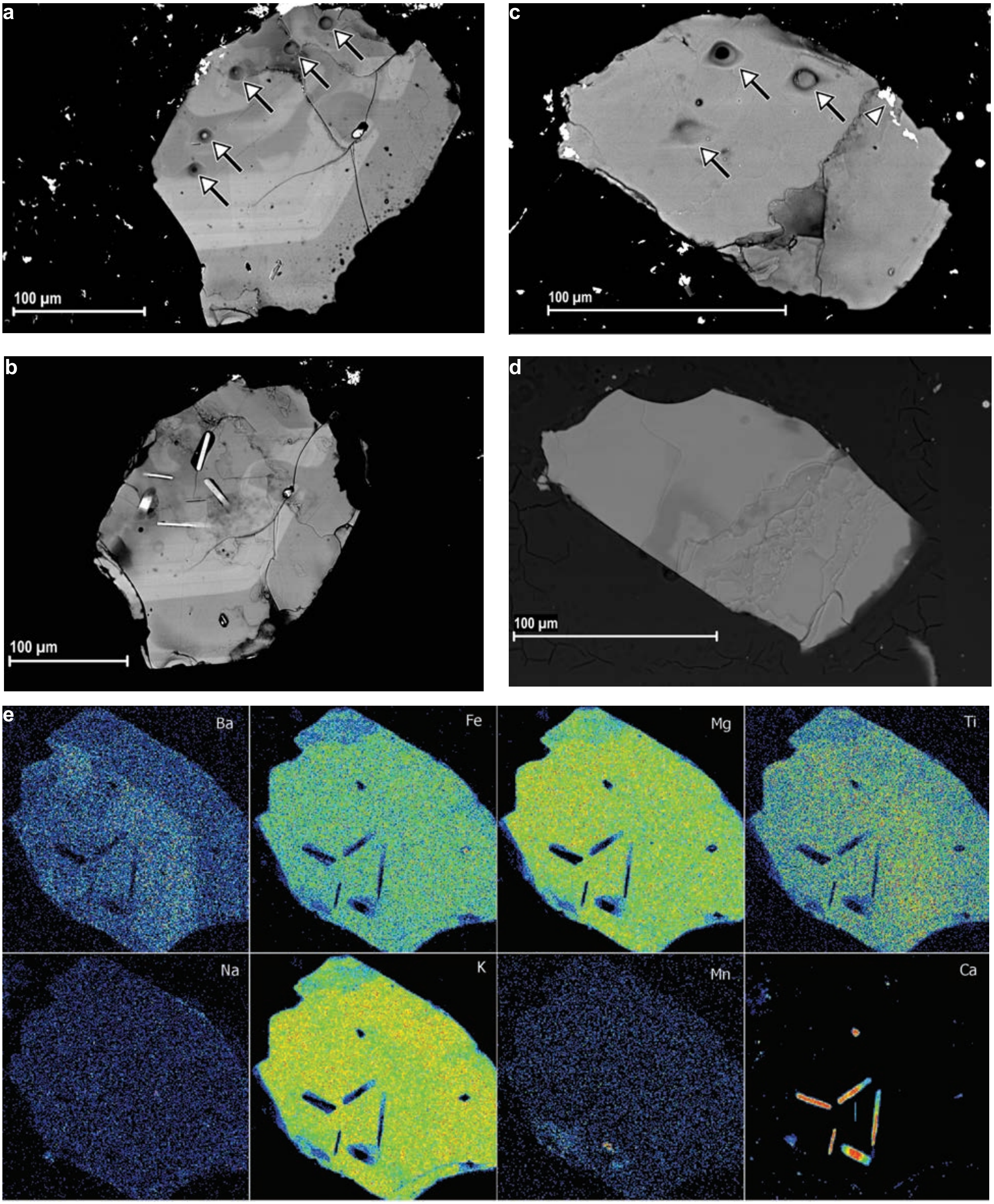

FIGURE 2. SEM-BSE images of two out of the seven analyzed samples. (**a**) BSE image of sample VUT191_11 after removal of Pt-coating. The SIMS craters are indicated by the arrows. The contrast due to chemical inhomogeneity (see text) is clearly visible; (**b**) BSE image of the sample VUT191_11 after further polishing by several micrometers to check for in depth inhomogeneity. Included phase is apatite; (**c**) BSE image of sample VUT187_13 after removal of Pt-coating; the white triangle with black borders indicates residues of Pt-coating; (**d**) BSE image of the sample VUT187_13 after further polishing by several micrometers; (**e**) X-ray maps of sample VUT191_11, showing Ba and Ti chemical zoning. Calcium is present in the apatite inclusions.

sample VUT0001_2, for which only one spot was allowed. Data in Table 3 were corrected in terms of H_2O for the effects due to the crystallographic orientation (Ottolini et al. 2002) since all the crystals in study were mounted in epoxy in planar position.

Light elements show greater variations among samples than within samples (Table 3). For example, average Li_2O concentrations varied from 0.001 (VUT187_13) to 0.027 wt% (PG5_1); F from 0.43 (VUT0001_2) to 1.29 wt% (VUT191_11); H_2O from 1.81 (VUT191_11) to 3.14 wt% (VUT0001_2). On the other hand, variation of H_2O is remarkable within samples VUT191_10 (from 1.72 to 2.50 wt%) and VUT187_24 (from 2.36 to 3.71 wt%), whereas Li_2O concentration significantly changes within sample PG5_1 (from 0.0095 to 0.0369 wt%). Furthermore, the two measured spots for VUT187_28 yielded notably different values for the F content (0.61 and 1.27 wt%). For more details on the samples chemical variability see the Discussion section below.

TABLE 3. Results of SIMS analyses

	Spot label	H_2O (wt%)	Li_2O (wt%)	F (wt%)
VUT 0001_2	a	3.30	0.0045	0.43
VUT 187_13	a	3.13	0.0012	0.552
VUT 187_13	b	3.15	0.0011	0.602
VUT 187_13	c	3.15	0.0009	0.637
Mean		3.14	0.00109	0.597
St.dev.		0.01	0.0002	0.042
VUT 187_24	a	2.36	0.0058	0.490
VUT 187_24	b	3.20	0.0045	0.478
VUT 187_24	c	3.26	0.0044	0.483
VUT 187_24	d	3.71	0.003	0.547
VUT 187_24	e	2.56	0.0033	0.523
Mean		3.02	0.0042	0.504
St.dev.		0.55	0.0011	0.03
VUT 187_28	a	2.86	0.0077	0.61
VUT 187_28	b	2.71	0.0102	1.27
Mean		2.79	0.0090	0.94
St.dev.		0.11	0.0018	0.47
VUT 191_10	a	1.72	0.016	0.96
VUT 191_10	b	2.41	0.0111	0.93
VUT 191_10	c	2.50	0.007	0.93
VUT 191_10	d	2.47	0.0061	0.97
VUT 191_10	e	2.42	0.0107	0.97
Mean		2.30	0.0102	0.95
St.dev.		0.33	0.0039	0.02
VUT 191_11	a	1.74	0.0075	1.33
VUT 191_11	b	1.80	0.0136	1.29
VUT 191_11	c	1.79	0.0156	1.25
VUT 191_11	d	2.08	0.0239	1.37
VUT 191_11	e	1.64	0.0104	1.22
Mean		1.81	0.0142	1.29
St.dev.		0.16	0.0062	0.06
PG5_1	a	2.90	0.0345	0.501
PG5_1	b	3.01	0.0369	0.534
PG5_1	c	3.23	0.0095	0.590
Mean		3.05	0.027	0.542
St.dev.		0.17	0.0152	0.04

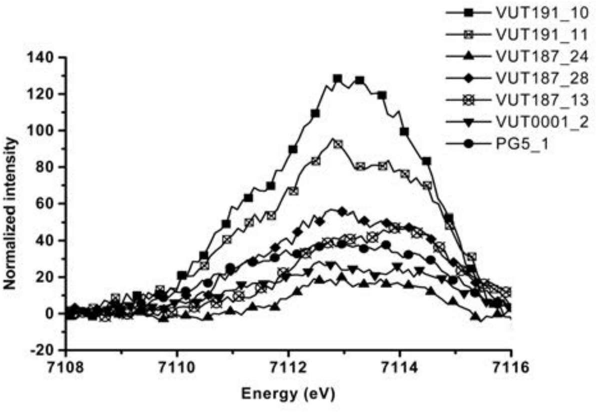

FIGURE 3. Fe *K* pre-edge spectra: comparison of all sample studied (run A only) using micro-XANES.

Micro-XANES

Micro-XANES results are illustrated in Figures 3–5 and reported in Table 4. Two spectra from each crystal at different (though unconstrained) orientations labeled A and B were acquired. XANES spectra of all samples in run A are shown in Figure 3. Note that although the beam was at the same orientation for all the "A" runs, the grains were randomly oriented relative to it. In Figure 4a, the full XANES spectrum is shown for sample VUT191_10. The features of the full spectrum are very close to those found for biotite in literature (Dyar et al. 2002a; Mottana et al. 2002). Note that in this spectrum the pre-edge (at ~7112 eV) is weak, contrary to what found in tetrahedral Fe^{3+}-bearing micas (Mottana et al. 2002). In Figure 4b, the A and B runs of the background subtracted pre-edge spectra for the same sample show different degrees of X-ray pleochroism due to differences in orientation, a behavior that is common to the other micas of the suite analyzed here (spectra not shown). Note also that the relative intensities of the two peaks at ~7111.4 and ~7113.4 eV (the latter is probably a doublet) vary with the orientation.

The pre-edge in each spectrum was fit with a single Gaussian curve, after background subtraction using techniques developed by Bajt et al. (1994). It is obvious from inspection of the plots in Figures 3 and 4b that these pre-edges are actually composites of several peaks that are resolved by using the higher-resolution Si(311) monochromator. However, because we did not orient the single crystals for this study and we did not have similarly oriented mica standards to calibrate them against, resolution of the individual features was not a priority for this project (though work is in progress to address exactly these issues, which requires a far more complicated experimental setup than the one used herein).

$Fe^{3+}/\Sigma Fe$ ratios were calculated employing the Bajt et al. (1994) calibration line for biotites and are compared in Table 4 with Mössbauer data. Previous work (Dyar et al. 2001) has established error bars of ±10–15% on determinations of $Fe^{3+}/\Sigma Fe$ for micas if single peak centroid fits and randomly oriented samples are used. The error arises because the single centroid is actually composed of several component peaks representing individual transitions, each of which is orientation-dependent (in a manner analogous to, for example, crystal field transitions). The effect of orientation was addressed by Dyar et al. (2002a), in a study of mica (and other) samples where single crystals were oriented such that the fixed beam would pass through the samples along the three known optical orientation directions. These measurements required a special experimental geometry (Dyar et al. 2002b) and the use of single crystals mounted on spindles and goniometer heads. Such special effort was needed, however, to constrain the amount of change in pre-edge structure

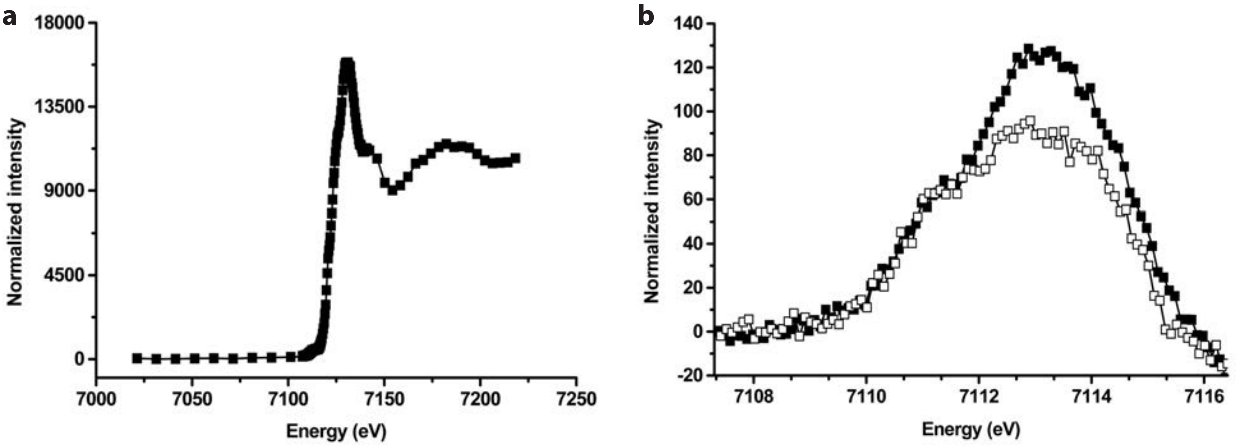

FIGURE 4. Micro-XANES spectra of sample VUT191_10. (**a**) The entire collected spectrum. (**b**) The extracted pre-edge region for runs A and B.

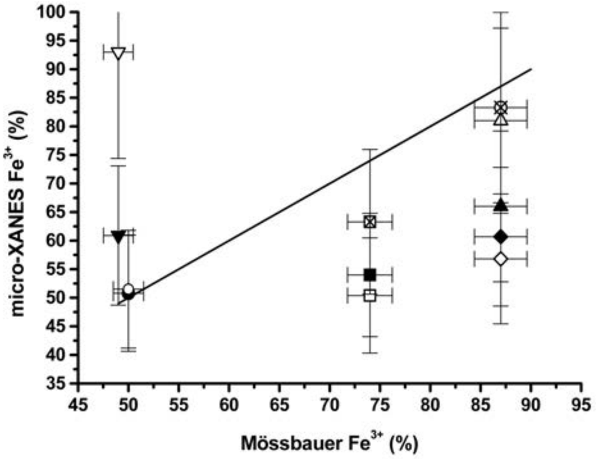

FIGURE 5. Comparison between Fe^{3+}% as determined by XANES and Mössbauer spectroscopy. Solid and crossed symbols = run A; empty circles = run B (see text for details). Sample identification as in the legend of Figure 3. The error bars are ±3% and ±20% for Mössbauer and XANES data respectively. The 1:1 line is shown.

TABLE 4. Fe^{3+}(%) as determined via XANES and Mössbauer

	Run	XANES	Mössbauer*
VUT0001_2	A	60.9	49.0
VUT0001_2	B	93.0	49.0
VUT187_13	A	83.3	87.0
VUT187_13	B	–	87.0
VUT187_24	A	66.0	87.0
VUT187_24	B	81.0	87.0
VUT187_28	A	60.7	87.0
VUT187_28	B	57.8	87.0
VUT191_10	A	54.0	74.0
VUT191_10	B	50.4	74.0
VUT191_11	A	63.3	74.0
VUT191_11	B	–	74.0
PG5_1	A	50.8	50.0
PG5_1	B	51.5	50.0

* Mössbauer data from Matarrese (2007) and from unpublished data.

that occurs as a function of optical orientation (i.e., X-ray pleochroism). For the micas measured in that study, the shift in the centroid of the extracted pre-edge corresponded to a difference of 6–21% absolute in the %Fe^{3+} (Table 4 of Dyar et al. 2002a). The pre-edge centroids of spectra acquired in the Z polarization direction were particularly distinct, as might be predicted from the crystal structure and refractive indices.

Structure refinement

Lattice parameters, including some details on data collection and summary results from structure refinements, are reported in Table 5 only for VUT0001_2 and PG5_1 samples. As detailed in the Materials and method section above, relevant data for VUT187_13, VUT187_24, and VUT187_28 are reported in Schingaro et al. (2007), whereas crystallographic data on VUT191_10 and VUT 191_11 are in Matarrese et al. (2008). Fractional atomic coordinates, partial occupancies, anisotropic and equivalent isotropic refinements are given in Table 6. Atomic labeling follows the conventions of Hazen and Burnham (1973). All the analyzed micas belong to the 1*M* polytype. In Tables 7 and 8 selected bond lengths and distortion parameters describing the polyhedral and layer geometry for the studied samples are provided. The refinements performed in space group *C*2/*m* converged at $3.08 \leq R \leq 3.63$, $3.32 \leq R_w \leq 3.98\%$.

In the final step of the anisotropic refinements, the hydrogen atom was added to the model. Its coordinates and occupancy were refined whereas the displacement parameters were constrained to be equal to those of the O4 atom. The final O-H distances were in the range 0.76(8)–0.87(5) Å.

In Table 9, the comparison between observed and calculated mean atomic numbers (m.a.n., e$^-$) as well as observed octahedral average bond distances and those calculated from the chemical molar fraction and atomic radii in Shannon (1976) is reported.

DISCUSSION

Chemical variability of the samples

The main chemical features of Vulture micas are the following: they are phlogopite-annite solid solutions with Fe/(Fe+Mg) in the range 0.10–0.40 apfu, Ti in the range 0.10–0.30 apfu, and Ba in the range 0.02–0.09 apfu. In addition, they are strongly oxidized, because Mössbauer investigation yielded Fe^{3+}/Fe$_{tot}$

from 0.40 to 0.88 over the whole suite of Vulture rocks (Matarrese 2007; Schingaro et al. 2007; Matarrese et al. 2008).

The samples selected for the present work are representative of the above general variability (see Table 1). The electron microprobe analyses (Table 1; Figures 1a–1e[1]) performed on the selected single crystals, generally show a low-to-moderate variability for major and minor constituents (i.e., those contributing to the structural formula) within each mineral grain. The coefficient of variation (CV), measured as 1σ% is less than 10% for Mg, Fe, and Ti data, expressed as oxide wt%. Specifically, CV is ≤4% for Mg, ≤3% for Fe and Ti. The most inhomogeneous sample is represented by VUT191_11, which exhibited both lateral and in depth inhomogeneity, see Figures 2a and 2b and X-ray maps for major/minor elements (Fig. 2e). For this sample, the CV is 12% for TiO_2 and 38% for BaO. Further EMP analyses performed on an inner layer of the crystal, after repolishing the sample surface (Fig. 2b), yielded for TiO_2 a CV of 9% and for BaO a CV of 27%.

TABLE 5. Crystal, experimental, and refinement data for 1 *M* phlogopite samples

	VUT0001_2	PG5_1
Space group	*C*2/*m*	*C*2/*m*
a (Å)	5.328(1)	5.337(1)
b (Å)	9.226(1)	9.235(1)
c (Å)	10.254(2)	10.256 (1)
β (°)	100.01(3)	100.00(1)
Cell volume (Å^3)	496.35(3)	497.81(12)
Z	2	2
Crystal size (mm)	0.51 × 0.38 × 0.02	0.23 × 0.26 × 0.02
θ range for data collection (°)	2–45	5–45
Reflections measured/unique/ R merging (R_{int})	12571/1956/ 0.065	18850/1904/ 0.104
Reflections used [I > 3σ(I)]	579	595
No. of refined parameters	73	71
Goof*	0.76	0.92
R_1†	3.08	3.63
R_w‡	3.32	3.98
$\Delta\rho_{min}$, $\Delta\rho_{max}$ (e/Å^3)	–0.20, 0.31	–0.53, 0.82

* Goodness-of-fit = $[\Sigma[w(F_o^2 - F_c^2)^2]/(N - P)]^{1/2}$, where *N* and *P* are the number of reflections and parameters, respectively.
† $R_1 = \Sigma[|F_o| - |F_c|]/\Sigma|F_o|$.
‡ $R_w = [\Sigma[w(|F_o| - |F_c|)^2]/\Sigma w(|F_o|)^2]^{1/2}$.

In terms of light elements, the CV (as 1σ%) in the SIMS data set for H_2O resulted to be: ~4% (VUT187_28), ~9% (VUT191_11), 14% (VUT191_10) up to 18% (VUT187_24). A CV on the order of 6% was obtained in PG5_1, whereas lower values resulted for VUT187_13. Remarkable variation in the ion signals for Li was found within a single crystal: in PG5_1 the Li content resulted 171.5 and 44.2 ppm in two close spots, while in VUT191_11 the Li contents ranged from 111 to 35 ppm over the five analyzed spots. Such a chemical heterogeneity was also documented for F. For instance, in VUT187_28 we got concentrations by 0.61 and 1.27 (wt%) F in two close micro-areas on the original sample surface. The reproducibility of analysis, investigated repeatedly in our standards elbaite and schorl, was on the order of 2% (as 1σ%) within a one-day analytical session. Because all the analyses were done over a one-day span, it is apparent that the mica crystals are characterized by an intrinsic micro-heterogeneity. This scatter was also apparent within single SIMS analysis (one spot) as a significant variation of the ion signals (H^+, Li^+, F^+) vs. time. This latter correlates to an in depth variation of the light element concentration over <1 μm, which represents the depth sampled by the ion beam bombardment under the present experimental conditions.

$Fe^{3+}/\Sigma Fe$ ratios from mica single crystals

Although spectra in Figures 3 and 4b were fit with Gaussian singlets to obtain $Fe^{3+}/\Sigma Fe$, the structure with the pre-edges is conspicuous. The bands at 7111.4, 7112.8, and 7114.1 eV are also observed in other trioctahedral micas (Dyar et al. 2002a). In our samples, bands at 7112.8 and 7114.1 are clearly resolved for samples VUT187_13, VUT187_28, and VUT191_11, even if their relative intensity changes from sample to sample. We do not yet have a theoretical (or even, an experimental) framework for interpretation of these bands or their assignment to specific transitions for particular sites, valence states, or optical orientations, though such work is underway.

TABLE 6. Results of structure refinement in space group *C*2/*m*: crystallographic coordinates, equivalent isotropic (Å^2), partial occupancies, and anisotropic displacement parameters

Site	Atom	*x*/*a*	*y*/*b*	*z*/*c*	$U_{iso/equiv}$	Occupancy	U_{11}	U_{22}	U_{33}	U_{23}	U_{13}	U_{12}
						Sample VUT0001_2						
K	K^+	0.0000	0.5000	0.0000	0.0350	1.0202(9)	0.0328(9)	0.0353(10)	0.0368(10)	0.0000	0.0058(8)	0.0000
M1	Mg^{2+}	0.0000	0.0000	0.5000	0.0137	0.8282(8)	0.0098(8)	0.0105(9)	0.0214(11)	0.0000	0.0041(7)	0.0000
	Fe^{2+}	0.0000	0.0000	0.5000	0.0137	0.1719(7)	0.0098(8)	0.0105(9)	0.0214(11)	0.0000	0.0041(7)	0.0000
M2	Mg^{2+}	0.0000	0.33464(16)	0.5000	0.0140	0.8224(8)	0.0091(5)	0.0144(6)	0.0184(6)	0.0000	0.0024(4)	0.0000
	Fe^{2+}	0.0000	0.33464(16)	0.5000	0.0140	0.1776(8)	0.0091(5)	0.0144(6)	0.0184(6)	0.0000	0.0024(4)	0.0000
T	Si, Si^{4+}	0.07548(14)	0.16683(11)	0.22660(8)	0.0134	0.9850(10)	0.0104(3)	0.0121(4)	0.0177(4)	0.0001(5)	0.0027(3)	0.0000(4)
O1	O,O^{2-}	0.3319(4)	0.2241(3)	0.1698(2)	0.0210	1.0000(8)	0.0172(10)	0.0244(13)	0.0218(11)	–0.0032(10)	0.0043(9)	–0.0044(10)
O2	O,O^{2-}	0.0050(7)	0.0000	0.1700(4)	0.0210	1.0002(8)	0.0239(17)	0.0159(16)	0.0220(17)	0.0000	0.0003(14)	0.0000
O3	O,O^{2-}	0.1304(4)	0.1675(3)	0.3916(2)	0.0145	1.0001(8)	0.0140(9)	0.0136(10)	0.0159(10)	–0.0009(11)	0.0028(8)	–0.0004(10)
O4	O,O^{2-}	0.1320(7)	0.5000	0.3992(4)	0.0151	1.0003(8)	0.0113(15)	0.0128(16)	0.0208(18)	0.0000	0.0021(14)	0.0000
	H	0.008(18)	0.5000	0.337(10)	0.0151	0.6346(10)	0.0113(15)	0.0128(16)	0.0208(18)	0.0000	0.0021(14)	0.0000
						Sample PG5_1						
K	K^+	0.0000	0.5000	0.0000	0.0295	0.9940(9)	0.0302(11)	0.0284(11)	0.0300(12)	0.0000	0.0057(9)	0.0000
M1	Mg^{2+}	0.0000	0.0000	0.5000	0.0098	0.7927(8)	0.0080(9)	0.0056(9)	0.0168(12)	0.0000	0.0049(8)	0.0000
	Fe^{2+}	0.0000	0.0000	0.5000	0.0098	0.2070(8)	0.0080(9)	0.0056(9)	0.0168(12)	0.0000	0.0049(8)	0.0000
M2	Mg^{2+}	0.0000	0.33403(18)	0.5000	0.0105	0.7927(8)	0.0082(6)	0.0094(6)	0.0144(7)	0.0000	0.0030(5)	0.0000
	Fe^{2+}	0.0000	0.33403(18)	0.5000	0.0105	0.2072(8)	0.0082(6)	0.0094(6)	0.0144(7)	0.0000	0.0030(5)	0.0000
T	Si, Si^{4+}	0.07560(17)	0.16686(12)	0.22671(10)	0.0094	0.9862(10)	0.0092(4)	0.0077(4)	0.0117(4)	–0.0001(6)	0.0029(3)	0.0004(5)
O1	O,O^{2-}	0.3312(5)	0.2237(4)	0.1696(3)	0.0186	1.0001(8)	0.0170(12)	0.0206(15)	0.0185(13)	–0.0017(12)	0.0041(11)	–0.0062(12)
O2	O,O^{2-}	0.0051(8)	0.0000	0.1698(4)	0.0180	1.0001(8)	0.023(2)	0.0113(17)	0.019(2)	0.0000	–0.0003(16)	0.0000
O3	O,O^{2-}	0.1306(5)	0.1674(4)	0.3918(3)	0.0114	1.0001(8)	0.0087(10)	0.0111(11)	0.0147(12)	0.0006(13)	0.0026(9)	–0.0007(11)
O4	O,O^{2-}	0.1327(8)	0.5000	0.3992(4)	0.0110	0.9999(8)	0.0126(19)	0.0121(19)	0.0082(18)	0.0000	0.0018(16)	0.0000
	H	0.118(15)	0.5000	0.325(8)	0.0110	0.9645(10)	0.0126(19)	0.0121(19)	0.0082(18)	0.0000	0.0018(16)	0.0000

Figure 5 compares the micro-XANES results with Mössbauer determinations of the Fe^{3+}/Fe_{tot} ratio from previous studies (Matarrese 2007; Schingaro et al. 2007; Matarrese et al. 2008) and unpublished data. Some of the sample measurements (VUT0001_2A, PG5_1A,B, VUT187_13A, VUT187_24B, and VUT191_11A) fall close to the 1:1 line, while others significantly depart from it. Because Mössbauer values are an "average" over several crystals, some single crystals may have quite distinct $Fe^{3+}/\Sigma Fe$ values that are not representative of the "average crystal." This may explain the different results for samples VUT187 and VUT191, which have geological histories consistent with large variations in crystallization/re-equilibration conditions (see section Crystal chemistry below).

It can also be seen that, when two measurements are available (A and B) for each sample, they are sometimes very close to each other (the case of samples PG5_1, VUT187_28, and VUT191_10), and sometimes not (VUT0001_2 and VUT187_24). It is unlikely that such differences are due to X-ray beam damaging or oxidizing effect on Fe, especially for

TABLE 7. Results of structure refinement in space group *C2/m*: selected bond distances (Å)

	VUT0001_2	PG5_1
T-O1	1.662(2)	1.660(3)
T-O1′	1.665(2)	1.674(3)
T-O2	1.665(2)	1.668(2)
T-O3	1.666(2)	1.667(3)
<T-O>	1.665	1.667
M1-O4(×2)	2.051(4)	2.051(4)
M1-O3(×4)	2.091(2)	2.092(3)
<M1-O>	2.078	2.078
M2-O4(×2)	2.035(3)	2.043(3)
M2-O3 (×2)	2.086(2)	2.087(3)
M2O3′(×2)	2.089(3)	2.088(3)
<M2-O>	2.070	2.073
<M-O>	2.073	2.075
K-O1(×4)	2.941(3)	2.941(3)
K-O1′(×4)	3.401(3)	3.405(3)
K-O2(×2)	2.944(4)	2.944(4)
K-O2′(×2)	3.405(4)	3.407(5)
$<K\text{-}O>_{inner}$	2.941	2.942
$<K\text{-}O>_{outer}$	3.402	3.406
<K-O>	3.172	3.174

TABLE 8. Selected parameters derived from the structure refinements in space group *C2/m*

	VUT0001_2	PG5_1
t_{tet} (Å)	2.239	2.244
BLD_T	0.083	0.209
$Volume_T$ (Å^3)	2.366	2.378
TQE	1.000	1.002
TAV	0.765	0.910
τ (°)	110.14	110.22
α (°)	10.13	10.15
Δz (Å)	0.002	0.002
D.M. (Å)	0.578	0.586
ΨM1 (°)	59.04	59.08
ΨM2 (°)	58.91	58.98
BLD_{M1}	0.860	0.868
ELD_{M1}	5.172	5.215
BLD_{M2}	1.113	0.940
ELD_{M2}	5.017	5.099
$Shift_{M2}$ (Å)	0.012	0.006
$Volume_{M1}$ (Å^3)	11.76	11.756
OQE_{M1}	1.012	1.012
OAV_{M1}	38.52	39.18
$Volume_{M2}$ (Å^3)	11.64	11.67
OQE_{M2}	1.011	1.012
OAV_{M2}	36.68	37.81
$e_u(M1)/e_s(M1)$	1.109	1.110
$e_u(M2)/e_s(M2)$	1.106	1.108
t_{oct} (Å)	2.138	2.136
t_{int} (Å)	3.431	3.427
ΔK-O (Å)	0.461	0.463
$t_{K\text{-}O4}$ (Å)	3.970	3.970

Notes: t_{tet} = tetrahedral sheet thickness calculated from z coordinates of basal and apical O atoms; TQE = tetrahedral quadratic elongation (Robinson et al. 1971); TAV = tetrahedral angle variance (Robinson et al. 1971); TAV = tetrahedral flattening angle; τ = tetrahedral rotation angle (Hazen and Burnham 1973); Δz = departure from co-planarity of the basal O atoms (Güven 1971); D.M. = dimensional misfit between tetrahedral and octahedral sheets (Toraya 1981); Ψ = octahedral flattening angles (Donnay et al. 1964a, 1964b); BLD = bond-length distortions (Renner and Lehmann 1986); ELD = edge-length distortion (Renner and Lehmann 1986); $Shift_{M2}$ = off-center shift of the M2 cation defined as the distance between the refined position of cation and the geometrical center of M2 site (coordinates: *x/a* = 0.0, *y/b* = 0.8333, *z/c* = 0.5); OQE = octahedral quadratic elongation (Robinson et al. 1971); OAV = octahedral angle variance (Robinson et al. 1971); e_u, e_s = mean lengths of unshared and shared edges (Toraya 1981), respectively; t_{oct} = octahedral sheet thickness (Toraya 1981); t_{int} = calculated from the *z* coordinates of basal O atoms; ΔK-O = <K-O>outer-<K-O>inner; $t_{K\text{-}O4}$ = projection of K-O4 distance along c*.

TABLE 9. Mean atomic numbers of cation sites (e^-) and octahedral and tetrahedral mean distances (Å), as determined by structure refinement and chemical analyses

	VUT0001_2	VUT187_13*	VUT187_24*	VUT187_28*	VUT191_10†	VUT191_11†	PG5_1
$e^-_{(M1)\ X\text{-ref}}$	14.41	14.63	14.92	14.53	16.77	16.35	14.89
$e^-_{(M2)\ X\text{-ref}}$	14.49	15.20	15.55	15.27	17.00	16.96	14.90
$e^-_{(M1+2M2)\ X\text{-ref}}$	43.39	45.03	46.02	45.07	50.77	50.27	44.69
$e^-_{(M1+2M2)\ EMPA1}$	43.49	44.34	45.49	44.58	48.77	48.77	44.47
$e^-_{(M1+2M2)\ EMPA2}$	42.96	–	45.12	44.66	48.89	–	44.46
$e^-_{(M1+2M2)\ EMPA3}$	43.41	45.06	45.88	45.14	50.82	49.06	44.37
K $e^-_{X\text{-ref}}$	19.38	19.05	19.29	19.63	21.06	21.32	18.89
K e^-_{EMPA3}	18.06	18.63	18.70	18.82	20.62	21.03	19.04
T $e^-_{X\text{-ref}}$	13.79	13.89	13.93	13.93	13.90	13.91	13.81
T e^-_{EMPA3}	13.67	13.67	13.68	13.68	13.66	13.67	13.68
$<M\text{-}O>_{X\text{-ref}}$	2.073	2.071	2.072	2.070	2.073	2.070	2.075
$<M\text{-}O>_{EMPA1}$	2.068	2.068	2.070	2.070	2.067	2.062	2.070
$<M\text{-}O>_{EMPA2}$	2.065	–	2.067	2.071	2.068	–	2.070
$<M\text{-}O>_{EMPA3}$	2.068	2.066	2.065	2.068	2.065	2.061	2.070
$<T\text{-}O>_{X\text{-ref}}$	1.665	1.667	1.665	1.664	1.666	1.667	1.667
$<T\text{-}O>_{EMPA1}$	1.668	1.669	1.667	1.667	1.670	1.668	1.667
$<T\text{-}O>_{EMPA2}$	1.668	–	1.667	1.667	1.670	–	1.667
$<T\text{-}O>_{EMPA3}$	1.668	1.668	1.667	1.666	1.669	1.668	1.667

Notes: EMPA1: from Table 2 = XANES (Run A); EMPA2: from Table 2 = XANES (Run B); EMPA3: from Table 10 (see the "Discussion: Crystal chemistry" section); X-ref: from structure refinement.

* X-ref data from Schingaro et al. (2007).

† X-ref data from Matarrese et al. (2008).

micas where the Fe oxidation is accompanied by deprotonation (see Ventruti et al. 2008 and references therein). Such effects have not been observed at the operating conditions normally used during the measurements at X26A and detailed in the Materials and methods section above (see also Cottrel et al. 2009). These differences can be largely explained as simply the effect of varying orientation in a non-systematic way, which is what fundamentally gives rise to the large error bars on these measurements (Dyar et al. 2002a).

However, in evaluating the XANES data, we cannot overlook the fact that the SIMS analyses of the samples revealed their heterogeneity at the micro-scale (see section above). It is interesting to note that the samples VUT191_11, VUT191_10, and VUT187_24, which exhibit major variability of the water content (see Table 3), are also among those displaying the greatest differences of $Fe^{3+}/\Sigma Fe$ values with the Mössbauer results or between the A and B orientations (see Fig. 5). It therefore seems likely that some of the variability of the Fe^{3+} content is also due to Fe^{3+}-zoning within crystals and from crystal to crystal.

Structural details

The structural parameters of the studied samples are consistent with those reported in the database of refinements of micas in the annite-phlogopite join (Brigatti and Guggenheim 2002). The analyzed micas are meso-octahedral from a geometrical point of view and homo-octahedral from a chemical point of view (Weiss et al. 1992; Ďurovíč 1994) as evidenced by the analysis of Tables 7 and 9.

Over the whole suite of samples considered, the *c*-parameter varies from 10.181(2) to 10.256(1) Å (see Table 5; Schingaro et al. 2007; Matarrese et al. 2008). As illustrated in Figure 6, there is a general trend for a decrease of the *c* with the water content, as previously reported (Cruciani and Zanazzi 1994). This shortening is associated with substitution at the O4 hydroxyl site, i.e., to OH ↔ F substitution (Boukili et al. 2001) and/or to deprotonation mechanisms (Cesare et al. 2003; Scordari et al. 2006; Sassi et al. 2008 and references therein). Several structural studies have shown that the deprotonation mechanism involving Ti, i.e., the Ti-oxy substitution, has distinctive structural manifestations such as: (1) shortening of the *c*-parameter as well as of the K-O4 distance; (2) decreasing M2-O4 distance; (3) increasing bond length distortions (BLD) for M2 site; (4) increasing values for the shift of the M2 cation from the geometric center of the octahedron toward the O4 oxygen; and (5) decreasing values for $\Delta_{K\text{-}O}$ and t_{int} (Cruciani and Zanazzi 1994; Cesare et al. 2003; Schingaro et al. 2005; Scordari et al. 2006, 2008). In addition, other parameters describing polyhedral and layer deformation related to the increase of the Ti concentration [for instance *y*(M2), *x*(O3)-*x*(O4), $(O3\text{-}O3)_{M1}$, and $(O3\text{-}O3)_{M2}$, c1+c2, etc.] are discussed in Brigatti et al. (2003). These have been used to gain insights into the crystal chemistry of micas (e.g., Schingaro et al. 2005; Mesto et al. 2006). Structural distortion induced by other kind of substitutions, such as Ti-vacancy or Fe^{3+}, Al^{3+}-oxy, have not all been specifically studied. Laurora et al. (2007), analyzing the crystal-chemical details of volcanic micas, argue that Fe^{3+}-oxy structural effects should be similar to those of Ti-oxy. The results of Matarrese (2007) are in partial agreement with those of Laurora et al. (2007) because cations like Ti and Fe^{3+}, Al^{3+} are often involved in multiple substitutions. Sassi et al. (2008) found that when substantial octahedral vacancy occurs in biotite, the structural effect of this substitution may be masked by the coexistence of the Ti-oxy mechanism. Other investigations on Vulture phlogopites (Matarrese et al. 2008; Scordari et al. 2008) have documented that different values of some structural features are observed in the case of prevalence of $M^{3+,4+}$-oxy substitutions, and in the case of prevalence of vacancy-bearing substitutions ($3^{VI}Fe^{2+} \rightarrow 2^{VI}Fe^{3+} + \square$ and/or $2^{VI}R^{2+} \leftrightarrow {}^{VI}Ti^{4+} + {}^{VI}\square$ substitutions) resulting in a bimodal behavior of the relevant parameters.

Very recently, Ventruti et al. 2008 have found that the effect of extensive Fe^{3+}-oxy substitutions lead to: abrupt changes of the *a*- and *b*-cell parameters; the enhancement of all structural distortions (see the list 1 to 5 above) indicative of Ti-oxy substitution.

In the Mt. Vulture samples studied here, the greater the oxy component, the higher the out-of-center-shift of the M2 cation (Fig. 7) and the distortion of the M2 site (Fig. 8). Only VUT0001_2 and PG5_1 have structural parameters consistent with a low oxy component. This is also confirmed by their final crystal-chemical formulas (see below), which show a different degree of hydrogenation from the other samples studied. Figure 9 illustrates that the distortion of the M1 site (as quantified by the c1+c2 parameter, see Fig. 9 caption) increases with the Ti concentration in the samples, confirming that the M1 site is affected by the composition of the M2 site (Brigatti et al. 2003).

It can be concluded that specific structural parameters (such as $shift_{M2}$ and BLD_{M2}) reflect the extent of deprotonation mechanism in the studied micas, whereas others (such as c1+c2) may vary remarkably depending on the chemistry of the particular sample (i.e., presence or absence of Li, vacancies, Fe^{2+}/Fe^{3+} ratio, etc.) and on the extent by which the substitutions affect the relative size of M1 and M2 sites.

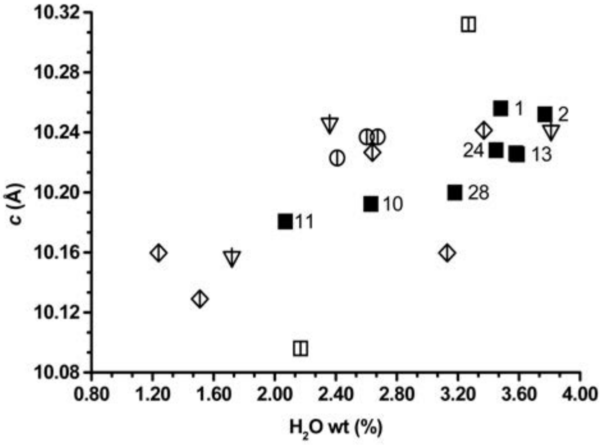

FIGURE 6. *c* vs. H_2O diagram for Vulture micas. Solid and crossed symbols: this work. Open symbols with vertical bar: literature data. In detail: squares = Mesto et al. (2006); circles = Scordari et al. (2006); triangles pointing upward = Schingaro et al. (2007); triangles pointing downward = Matarrese et al. (2008); diamonds = Scordari et al. (2008). In the figure sample names have been shortened as follows: 1 indicates sample PG5_1, 2 indicates sample VUT0001_2, etc.

Crystal chemistry

The final structural formulas are reported in Table 10. Initial crystal-chemical formulas in Table 2 have been calculated on the basis of 12 (O, OH, F, Cl) by combining EMPA, XANES, and SIMS data. XANES data obtained from two different orientations relative to the X-ray beam are labeled XANES (Run A) and XANES (Run B), respectively. In Table 9, the mean atomic numbers (e^-) observed from structure refinements [rows e^-(M1, M2, M1+2M2)$_{\text{X-ref}}$] are compared with those calculated from formulas in Table 2 relevant to XANES (Run A) data (subscript EMPA1) and XANES (Run B) data (subscript EMPA2) and from formulas in Table 10 (subscript EMPA3). Table 9 reveals that not all the formulas in Table 2 are acceptable because the relevant calculated mean atomic number for the octahedral sites (M1+2M2) is not in agreement with the refined value (X-ref). The commonly accepted average error associated the refined site scattering power (or mean atomic number) is ~0.5 e^-, whereas the differences in Table 9 between X-ref data and EMPA1,2 data range between ~0.05 and ~2 e^-. Besides the analytical uncertainties of the EMPA data, source of errors may be related to the H_2O intragranular variations and/or problems in the determination of Fe^{2+}/Fe^{3+} ratio, which may affect to various extents, the concentration of octahedral vacancies. For example, it can easily be demonstrated that, all other variables being the same, varying the Fe^{2+}% from 0 to 100% in the derivation of a crystal-chemical formula makes the mean atomic number vary by about 3 e^-.

In Table 2, two sets of values are provided for the OH$^-$ content: one is that measured by SIMS, the other is that estimated by structural data [equation $c = 10.065(16) + 0.125(13)$OH, from Ventruti et al. (2008)]. Most of them agree within at 1–3σ% of the SIMS analytical errors for H_2O. On the other hand, recent Mössbauer investigations (Scordari et al. 2006; Matarrese 2007; Matarrese et al. 2008) as well as unpublished data have suggested that Mt. Vulture phlogopites are generally Fe^{3+}-rich, with Fe^{3+} varying in the range 40 to 87%. Table 4 and Figure 4 demonstrate that not all XANES measurements of our samples yielded results similar to the Mössbauer values. This may indicate intracrystalline variability of Fe^{2+}/Fe^{3+} ratio, or it may be attributed to analytical error arising from orientation effects. It has also to be taken into account that recent micro-FTIR investigations (Scordari et al. 2006, 2008; Lacalamita 2009) have shown that generally in brown micas from Mt. Vulture (such as those here considered) octahedral vacancies are absent or negligible.

On the basis of all the above considerations, the final structural formulas, shown in Table 10, were determined using the following criteria: (1) formulas from Table 2 were considered acceptable only if, for the octahedral sites (M1+2M2), the difference Δm.a.n. = m.a.n.$_{\text{(EMPA)}}$-m.a.n.$_{\text{(X-ref)}}$ was <1.0 e^- (which means

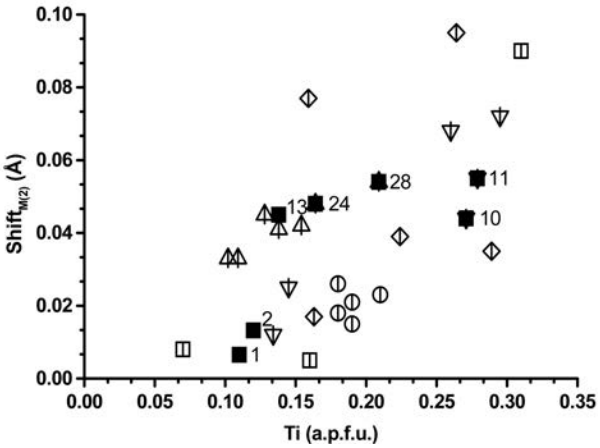

FIGURE 7. Shift$_{M2}$ vs. Ti diagram. High values of the shift$_{M2}$ parameter are associated to the occurrence of Ti-oxy substitutions (see text). Legend as in Figure 6.

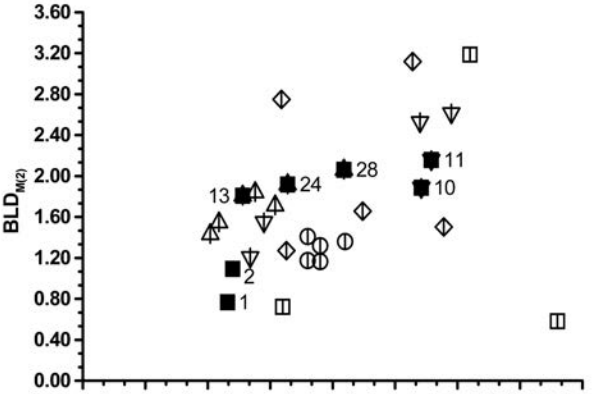

FIGURE 8. BLD$_{M2}$ vs. Ti diagram. The higher the Ti-oxy component, the more distorted is the M2 site. Legend as in Figure 6.

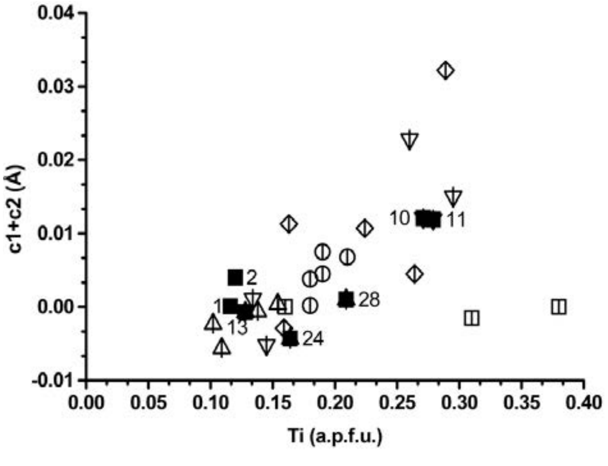

FIGURE 9. c1+c2 vs. Ti diagram. The relationships defining c1 and c2 parameters are

$$c1 = 2 \cdot y(\mathrm{O3}) \cdot b - \frac{1}{2} \cdot \sqrt{\left(a^2 + 4 \cdot y(\mathrm{O3}) \cdot b^2\right)}$$

and

$$c2 = -\left[\frac{a^2}{\sqrt{\left(a^2 + 4 \cdot y(\mathrm{O3}) \cdot b^2\right)}}\right] \cdot \left[x(\mathrm{O3}) - x(\mathrm{O4})\right]$$

(Brigatti et al. 2003), where *a* and *b* are cell parameters and *x*(O3), *y*(O3), and *x*(O4) are fractional coordinates of the relevant oxygen atoms, obtained from structure refinement. Legend as in Figure 6.

TABLE 10. Final structural formulas for the study samples

	Interlayer site	Octahedral site	Tetrahedral site	Anionic site
VUT0001_2	$(K_{0.81}Na_{0.09}Ba_{0.03}\square_{0.08})$	$(Al_{0.17}Mg_{2.26}Fe^{2+}_{0.17}Fe^{3+}_{0.27}Ti_{0.12}\square_{0.01})$	$(Si_{2.69}Al_{1.31})$	$O_{10.31}F_{0.10}OH_{1.59}$
VUT187_13	$(K_{0.82}Na_{0.11}Ba_{0.04}\square_{0.03})$	$(Al_{0.12}Mg_{2.19}Mn_{0.01}Fe^{2+}_{0.09}Fe^{3+}_{0.46}Ti_{0.13})$	$(Si_{2.67}Al_{1.33})$	$O_{10.52}F_{0.14}OH_{1.34}$
VUT187_24	$(K_{0.83}Na_{0.11}Ba_{0.03}\square_{0.03})$	$(Al_{0.12}Mg_{2.07}Mn_{0.01}Fe^{2+}_{0.12}Fe^{3+}_{0.49}Ti_{0.16}\square_{0.03})$	$(Si_{2.72}Al_{1.28})$	$O_{10.59}F_{0.12}Cl_{0.01}OH_{1.28}$
VUT187_28	$(K_{0.83}Na_{0.10}Ba_{0.04}\square_{0.03})$	$(Al_{0.11}Mg_{2.17}Mn_{0.01}Fe^{2+}_{0.19}Fe^{3+}_{0.30}Ti_{0.21}\square_{0.01})$	$(Si_{2.73}Al_{1.27})$	$O_{10.53}F_{0.22}OH_{1.25}$
VUT191_10	$(K_{0.81}Na_{0.09}Ba_{0.07}\square_{0.03})$	$(Al_{0.12}Mg_{1.83}Mn_{0.01}Fe^{2+}_{0.35}Fe^{3+}_{0.41}Ti_{0.27}\square_{0.01})$	$(Si_{2.64}Al_{1.36})$	$O_{10.73}F_{0.24}Cl_{0.01}OH_{1.02}$
VUT191_11	$(K_{0.78}Na_{0.09}Ba_{0.09}Ca_{0.01}\square_{0.03})$	$(Al_{0.14}Mg_{1.73}Mn_{0.01}Fe^{2+}_{0.28}Fe^{3+}_{0.49}Ti_{0.28}Li_{0.05}\square_{0.02})$	$(Si_{2.68}Al_{1.32})$	$O_{10.80}F_{0.32}Cl_{0.01}OH_{0.87}$
PG5_1	$(K_{0.85}Na_{0.11}Ba_{0.03}\square_{0.01})$	$(Al_{0.19}Mg_{2.10}Mn_{0.01}Fe^{2+}_{0.26}Fe^{3+}_{0.27}Ti_{0.12}Li_{0.01}\square_{0.04})$	$(Si_{2.71}Al_{1.29})$	$O_{10.31}F_{0.13}OH_{1.56}$

an error of 0.33 e^- per site); (2) if Δm.a.n. > 1.0 and in all cases of not-negligible content of octahedral vacancies, the formula is recalculated by varying the H_2O concentration to minimize octahedral vacancies and using charge-balance considerations; (3) in case of very different values of Fe^{3+} between A and B measurements from XANES, the value that leads to the best agreement with m.a.n.$_{(X\text{-ref})}$ upon application of criteria 1 and 2 above was selected for the final formula. The formulas in Table 10 lead to values labeled EMPA3 in Table 9; note the very good agreement not only between observed and calculated mean atomic numbers, with differences in the range 0.05–1.21 e^-, but also between observed distances and calculated ones using ionic radii from Shannon (1976).

The formulas in Table 10 are also consistent with the observed structural distorsions of the study micas: note, for instance, that in Figures 6–8, VUT0001 and PG5 are the most hydrogenated samples of the suite, and plot at opposite sides from VUT191_10 and _11, which are the most dehydrogenated samples. This correlates with the fact that VUT0001 and PG5 have, on average 1.58 OH^- groups per formula units (gpfu) and 0.31 excess oxygen apfu due to Ti^{4+} and Fe^{3+}-oxy substitutions, whereas VUT191_10 and VUT191_11 have on average 0.98 OH^- gpfu and 0.77 excess oxygen apfu. Note also that the OH^- gpfu in the final formulas (Table 10) are much closer to those expected from the *c*-cell parameter than the initial ones (see Table 2). Finally based on new SIMS and the micro-XANES contribution, the crystal-chemical formulas for samples VUT187_24 and VUT191_10 have been here significantly revised with respect to previous works (Schingaro et al. 2007; Matarrese et al. 2008).

Of all the H_2O SIMS data of this study, only the water contents pertaining to VUT187_13 and VUT187_28 are higher than 3σ% level, and appear to be overestimated by 10–15%. This discrepancy may be due to both the difference in sampled volumes during EMP and SIMS analysis and to the Fe oxidation states that were demonstrated to affect the ionization of H in silicates. In any case, such an uncertainty is comparable to the overall analytical error for H_2O measurements by SIMS in mica minerals (Ottolini et al. 2002).

For samples VUT187_28 and VUT191_10, the Fe^{3+}% differs from the Mössbauer value by ~30%. In these two cases, it is likely that the samples are affected by variation of the Fe^{3+} content at the micrometer scale and that the Mössbauer-measured Fe^{2+}/Fe^{3+} (see also Table 4) represents an average value. This conclusion could hold also for sample VUT187_24, whose H_2O content shows great variability (CV = 18%), which is not due to OH ↔ F substitution, since F from SIMS has CV = 6%. This was expected because previous investigations have shown that the relevant host rocks underwent post-magmatic oxidation (VUT187 host rock; Schingaro et al. 2007) or have been subjected to variable crystallization environment due to rapid magma ascent from to mantle up to HT/LP subvolcanic conditions (VUT191 host rock; Matarrese et al. 2008).

CONCLUDING REMARKS

A combination of chemical, structural, and spectroscopic single-crystal techniques allows a complete crystal-chemical characterization of the analyzed samples. Five crystals show an H_2O content in accord within 1–3σ% with that derived by *c*-parameter (Ventruti et al. 2008). A discrepancy by ~10–15% for SIMS analysis of H_2O in VUT187_13 and VUT187_28 may be attributed to residual matrix effects affecting the H^+ (relative to Si^+) ionization, both due to Fe and Ti contents, as well as to the Fe oxidation state in the sample (see Ottolini and Hawthorne 2001; Ottolini et al. 2002; Kogarko et al. 2005). The analytical errors by 10–20% of other non-routine single-crystal techniques, such as micro-XANES as well as sample characteristics (symmetry, shape, chemical inhomogeneity, etc.) may complicate the accurate determination of cation site population. However, high-quality structural data in association with those derived by in situ techniques allow sample heterogeneity to be characterized at the micrometer scale; this capability is invaluable for the study of "difficult" mineral phases such as volcanic micas. In the case of Vulture phlogopite, the chemical behavior ranges from homogeneous (Scordari et al. 2006) to markedly inhomogeneous (Matarrese et al. 2008; Scordari et al. 2008). A systematic study of the inhomogeneous samples at the micrometer scale can provide insightful relationships between their crystal chemistry and their associated volcanic history.

This study also makes apparent that the limitations of the micro-XANES technique can be minimized if there are known orientations in the standards and unknowns (Dyar et al. 2002b). Helpful lines of research in this regard are currently being pursued: using either micro-XRD instruments or synchrotron micro-XRD to determine crystallographic orientations on every grain analyzed in situ, and using electron backscatter diffraction (a technology that is becoming more accessible) to constrain crystal orientation. When combined with the use of high-resolution Si(311) monochromators to better resolve individual transitions, these methods may eventually allow us to match spectra of standards and unknowns at the same orientations, eliminating or reducing the effects of differential orientations. Along with further studies of the detailed structure (i.e., the component peaks in the pre-edge, each of which is caused by a particular transition), it should soon be possible to greatly reduce error bars on XANES measurements of Fe^{3+}.

ACKNOWLEDGMENTS

The authors are grateful to Marcello Serracino for assistance during electron probe microanalyses at the CNR-Istituto di Geologia Ambientale e Geoingegneria, Roma, and to Stefano Poli, Università di Milano, for X-ray elemental maps. Pasquale Trotti, Dipartimento Geomineralogico, Università di Bari, is acknowledged for technical management of the SEM images. Thanks are due to an anonymous referee and particularly to the Associate Editor Darrell Henry whose insightful suggestions remarkably improved this manuscript. This work was supported by the COFIN-MIUR and by the U.S. National Science Foundation, grant EAR-0809459 to M.D.D.

REFERENCES CITED

Bajt, S., Sutton, S.R., and Delaney, J.S. (1994) Microanalysis of iron oxidation states in silicates and oxides using X-ray absorption near-edge structure (XANES). Geochimica et Cosmochimica Acta, 58, 5209–5214.

Betteridge, P.W., Carruthers, J.R., Copper, R.I., Prouth, K., and Watkin, D.J. (2003) Crystals version 12: Software for guided crystal structure analysis. Journal of Applied Crystallography, 36, 1487–1492.

Bohlen, S.R., Peacor, D.R., and Essene, E.J. (1980) Crystal chemistry of a metamorphic biotite and its significance in water barometry. American Mineralogist, 65, 55–62.

Boukili, B., Robert, J.L., Beny, J.M., and Holtz, F. (2001) Structural effects of OH→F substitution in trioctahedral micas of the system: K_2O-FeO-Fe_2O_3-Al_2O_3-SiO_2-H_2O-HF. Schweizerische Mineralogische und Petrographische Mitteilungen, 81, 55–67.

Brigatti, M.F. and Guggenheim, S. (2002) Mica crystal chemistry and the influence of pressure, temperature, and solid solution on atomistic models. In A. Mottana, F.P. Sassi, J.B. Thompson, and S. Guggenheim, Eds., Micas: Crystal chemistry and metamorphic petrology, 46, p. 1–100. Reviews in Mineralogy and Geochemistry, Mineralogical Society of America, Chantilly, Virginia.

Brigatti, M.F., Guggenheim, S., and Poppi, L. (2003) Crystal chemistry of the 1*M* mica polytype: The octahedral sheet. American Mineralogist, 88, 667–675.

Brigatti, M.F., Caprilli, E., Funiciello, R., Giordano, G., Mottana, A., and Poppi, L. (2005) Crystal chemistry of ferroan phlogopites from the Albano maar lake zone (Colli Albani volcano, central Italy). European Journal of Mineralogy, 17, 611–621.

Bruker (2003a) APEX2. Bruker AXS Inc., Madison, Wisconsin, U.S.A.

——— (2003b) SAINT. Bruker AXS Inc., Madison, Wisconsin, U.S.A.

Buettner, A., Principe, C., Villa, I.M., and Bocchini, D. (2006) Geocronologia ^{39}Ar-^{40}Ar del Monte Vulture. In C. Principe, Ed., La Geologia del Monte Vulture, CNR–Regione Basilicata, p. 73–86. Grafiche Finiguerra, Lavello (Potenza, Italy).

Cesare, B., Cruciani, G., and Russo, U. (2003) Hydrogen deficiency in Ti-rich biotite from anatectic metapelites (El Joyazo, SE Spain): Crystal-chemical aspects and implications for high-temperature petrogenesis. American Mineralogist, 88, 583–595.

Cesare, B., Satish-Kumar, M., Cruciani, G., Pocker, S., and Nodali, L. (2008) Mineral chemistry of Ti-rich biotite from pegmatite and metapelitic granulites of the Kerala Khondalite Belt (southeast India): Petrology and further insight into titanium substitutions. American Mineralogist, 93, 327–388.

Cottrel, E., Kelley, K.A., Lanzirotti, A., and Fischer, R.A. (2009) High-precision determination of iron oxidation state in silicate glasses using XANES. Chemical Geology, 268, 167–179.

Cruciani, G. and Zanazzi, P.F. (1994) Cation partitioning and substitution mechanism in 1*M* phlogopite: A crystal chemical study. American Mineralogist, 79, 289–301.

Delaney, J.S., Sutton, S.R., and Dyar, M.D. (1996) In situ microanalysis of Fe^{3+}/ΣFe in amphibole by X-ray absorption near edge structure (XANES) spectroscopy. In M.D. Dyar, C. McCammon, and M.W. Schaefer, Eds., Mineral Spectroscopy: A tribute to Roger Burns, 5, p. 165–171. Geochemical Society, Houston, Texas.

Donnay, G., Morimoto, N., Takeda, H., and Donnay, J.D.H. (1964a) Trioctahedral one-layer micas. I. Crystal structure of a synthetic iron mica. Acta Crystallographica, 17, 1369–1373.

Donnay, G., Donnay, J.D.H., and Takeda, H. (1964b) Trioctahedral one-layer micas. II Prediction of the structure from composition and cell dimensions. Acta Crystallographica, 17, 1374–1381.

Ďurovíč, S. (1994) Classification of phyllosilicates according to the symmetry of their octahedral sheets. Ceramics-Silikàty, 38, 81–84.

Dyar, M.D. (2002) Optical and Mössbauer spectroscopy of iron in micas. In A. Mottana, F.P. Sassi, J.B. Thompson, and S. Guggenheim, Eds., Micas: Crystal chemistry and metamorphic petrology, 46, p. 313–340. Reviews in Mineralogy and Geochemistry, Mineralogical Society of America, Chantilly, Virginia.

Dyar, M.D., Colucci, M.T., and Guidotti, C.V. (1991) Forgotten major elements: Hydrogen and oxygen variation in biotite from metapelite. Geology, 19, 1029–1032.

Dyar, M.D., Guidotti, C.V., Holdaway, M.J., and Colucci, M. (1993) Nonstoichiometric hydrogen contents in common rock-forming hydrous silicates. Geochimica et Cosmochimica Acta, 57, 2913–2918.

Dyar, M.D., Delaney, J.S., and Sutton, S.R. (2001) Fe XANES spectra of iron-rich micas. European Journal of Mineralogy, 13, 1079–1098.

Dyar, M.D., Gunter, M.E., Delaney, J.S., Lanzarotti, A., and Sutton, S.R. (2002a) Systematics in the structure and XANES spectra of pyroxenes, amphiboles, and micas. Canadian Mineralogist, 40, 1375–1393.

——— (2002b) Use of the spindle stage for orientation of single crystals for microXAS: Isotropy and anisotropy in Fe-XANES spectra. American Mineralogist, 87, 1500–1504.

Fabbrizio, A., Rouse, J.P., and Carroll, M.R. (2006) New experimental data on biotite+magnetite+sanidine saturated phonolitic melts and application to the estimation of magmatic water fugacity. American Mineralogist, 91, 1863–1870.

Fabbrizio, A., Scaillet, B., and Carrol, M.R. (2009) Estimation of pre-eruptive magmatic water fugacity in the Phlegrean Fields, Naples, Italy. European Journal of Mineralogy, 21, 107–116.

Feldstein, S.N., Lang, R.A., Vennemann, T., and O'Neil, J.R. (1996) Ferric-ferrous ratios, H_2O contents and D/H ratios of phlogopite and biotite from lavas of different tectonic regimes. Contributions to Mineralogy and Petrology, 126, 51–66.

Forbes, W.C. and Flower, M.F.J. (1974) Phase relations of titan-phlogopite, $K_2Mg_4TiAl_2Si_6O_{20}(OH)_4$: A refractory in the upper mantle? Earth and Planetary Science Letters, 22, 60–66.

Güven, N. (1971) The crystal structure of 2M_1 phengite and 2M_1 muscovite. Zeischrift für Kristallographie, 134, 196–212.

Hazen, R.M. and Burnham, C.W. (1973) The crystal structure of one layer phlogopite and annite. American Mineralogist, 58, 889–900.

Henry, D.J. and Guidotti, C.V. (2002) Titanium in biotite from metapelitic rocks: Temperature effects, crystal-chemical controls, and petrologic applications. American Mineralogist, 87, 375–382.

Henry, D.J., Guidotti, C.V., and Thompson, J. (2005) The Ti-saturation surface for low-to-medium pressure metapelitic biotites: implications for geothermometry and Ti-substitution mechanisms. American Mineralogist, 90, 316–328.

Kogarko, L.N., Uvarova, Y.A., Sokolova, E., Hawthorne, F.C., Ottolini, L., and Grice, J.D. (2005) Oxykinoshitalite, a new species of mica from Fernando De Norohna Island, Pernambuco, Brazil: Occurrence and crystal structure. Canadian Mineralogist, 43, 1501–1510.

Lacalamita, M. (2009) Studio chimico-strutturale dei siti anionico e cationici in miche triottaedriche a temperature ambiente e non, 228 p. Ph.D. thesis, University of Bari, Italy.

Laurora, A., Brigatti, M.F., Mottana, A., Malferrari, D., and Caprilli, E. (2007) Crystal chemistry of trioctahedral micas in alcaline and subalkaline volcanic rocks: A case study from Mt. Sassetto (Tolfa district, Latium, central Italy). American Mineralogist, 92, 468–480.

Matarrese, S. (2007) Cristallochimica comparativa di flogopiti del Monte Vulture, 170 p. Ph.D. thesis, University of Bari, Italy.

Matarrese, S., Schingaro, E., Scordari, F., Stoppa, F., Rosatelli, G., Pedrazzi, G., and Ottolini, L. (2008) Crystal chemistry of phlogopite from Vulture-S.Michele subsynthem volcanics (Mt. Vulture, Italy) and volcanological implications. American Mineralogist, 93, 426–437.

Mesto, E., Schingaro, E., Scordari, F., and Ottolini, L. (2006) Electron probe microanalysis, secondary ion mass spectrometry and single crystal X-ray diffraction study of phlogopites from Mt. Vulture, Potenza, Italy: Consideration of cation partitioning. American Mineralogist, 91, 182–190.

Mottana, A., Marcelli, A., Cibin, G., and Dyar, M.D. (2002) X-ray absorption spectroscopy of the Micas. In A. Mottana, F.P. Sassi, J.B. Thompson, and S. Guggenheim, Eds., Micas: Crystal chemistry and metamorphic petrology, 46, p. 371–411. Reviews in Mineralogy and Geochemistry, Mineralogical Society of America, Chantilly, Virginia.

Ottolini, L. and Hawthorne, F.C. (2001) SIMS ionization of hydrogen in silicates: A case study of kornerupine. Journal of Analytical Atomic Spectrometry, 6, 1266–1270.

Ottolini, L., Bottazzi, P., and Vannucci, R. (1993) Quantification of lithium, beryllium and boron in silicates by secondary ion mass spectrometry using conventional energy filtering. Analytical Chemistry, 65, 1960–1968.

Ottolini, L., Bottazzi, P., Zanetti, A., and Vannucci, R. (1995) Determination of hydrogen in silicates by secondary ion mass spectrometry. Analyst, 120, 1309–1313.

Ottolini, L., Cámara, F., Hawthorne, F.C., and Stirling, J. (2002) SIMS matrix effects in the analysis of light elements in silicate minerals: Comparison with SREF and EMPA data. American Mineralogist, 87, 1477–1485.

Petit, P.-E., Farges, F., Wilke, M., and Solé, V.A. (2001) Determination of the iron oxidation state in Earth materials using XANES pre-edge information. Journal of Synchrotron Radiation, 8, 952–954.

Pouchou, J.L. and Pichoir, F. (1985) "PAP" $\Phi(\rho Z)$ procedure for improved quantitative micro-analysis. Microbeam Analysis, 104–160.

Renner, B. and Lehmann, G. (1986) Correlation of angular and bond length distortions in TO_4 units in crystals. Zeitschrift für Kristallographie, 175, 43–59.

Righter, K., Dyar, M.D., Delaney, J.S., Vennemann, T.W., Hervig, R.L., and King, P.L. (2002) Correlations of octahedral cations with OH^-, O^{2-}, Cl^-, and F^- in biotite from volcanic rocks and xenoliths. American Mineralogist, 87, 142–153.

Robert, J.L. (1976) Titanium solubility in synthetic phlogopite solid solution. Chemical Geology, 17, 213–227.

Robinson, K., Gibbs, G.V., and Ribbe, P.H. (1971) Quadratic elongation, a quantitative measure of distortion in coordination polyhedra. Science, 172, 567–570.

Sassi, R., Cruciani, G., Mazzoli, C., Nodali, L., and Craven, J. (2008) Multiple titanium substitutions in biotites from high-grade metapelitic xenoliths (Euganean Hills, Italy): Complete crystal chemistry and appraisal of petrologic control. American Mineralogist, 93, 339–350.

Schingaro, E., Scordari, F., Mesto, E., Brigatti, M.F., and Pedrazzi, G. (2005) Cation site partitioning in Ti-rich micas from Black Hill (Australia): A multi-technical approach. Clays and Clay Minerals, 53, 179–189.

Schingaro, E., Matarrese, S., Scordari, F., Rosatelli, G., Stoppa, F., and Pedrazzi, G. (2007) Crystal chemistry of trioctahedral micas from the Ventaruolo subsynthem volcanics (Mt. Vulture, Italy). Mineralogical Magazine, 71, 519–537.

Scordari, F., Ventruti, G., Sabato, A., Bellatreccia, F., Della Ventura, G., and Pedrazzi, G. (2006) Ti-rich phlogopite from Monte Vulture (Potenza, Italy) investigated by a multianalytical approach: Substitutional mechanisms and orientation of the OH dipoles. European Journal of Mineralogy, 18, 379–391.

Scordari, F., Schingaro, E., Ventruti, G., Lacalamita, M., and Ottolini, L. (2008) Red micas from basal ignimbrites of Mt. Vulture (Italy): Interlayer content appraisal by a multi-methodic approach. Physics and Chemistry of Minerals, 35, 163–174.

Shabani, A.A.T., Lalonde, A.E., and Whalen, J.B. (2003) Composition of biotite from granitic rocks of the canadian Appalachian orogen: A potential tectonomagmatic indicator? Canadian Mineralogist, 41, 1381–1396.

Shannon, R.D. (1976) Revised effective ionic radii and systematic studies of interatomic distances in halides and chalcogenides. Acta Crystallographica, A32, 751–767.

Sheldrick, G.M. (2003) SADABS, Program for empirical absorption correction of area detector data. University of Göttingen, Germany.

Stoppa, F., Rosatelli, G., and Principe, C. (2006) Classificazione modale delle vulcaniti del Monte Vulture. In C. Principe, Ed., La geologia del Monte Vulture, CNR–Regione Basilicata, p. 87–103. Grafiche Finiguerra, Lavello (Potenza, Italy).

Toraya, H. (1981) Distortions of octahedra and octahedral sheets in 1*M* micas and the relation to their stability. Zeitschrift für Kristallographie, 157, 173–190.

Ventruti, G., Zema, M., Scordari, F., and Pedrazzi, G. (2008) Thermal behavior of a Ti-rich phlogopite from Mt. Vulture (Potenza, Italy): An in situ X-ray single-crystal diffraction study. American Mineralogist, 93, 632–643

Virgo, D. and Popp, R.K. (2000) Hydrogen deficiency in mantle-derived phlogopites. American Mineralogist, 85, 753–759.

Waters, D.J. and Charnley, N.R. (2002) Local equilibrium in polymetamorphic gneiss and the titanium substitution in biotite. American Mineralogist, 87, 383–396.

Weiss, Z., Rieder, M., and Chmíelovà, M. (1992) Deformation of coordination polyhedra and their sheets in phyllosilicates. European Journal of Mineralogy, 4, 665–682.

Wilke, M., Farges, P.-E., Brown, Jr., G.E., and Martin, F. (2001) Oxidation state and coordination of Fe in minerals: An Fe *K*-XANES spectroscopic study. American Mineralogist, 86, 714–730.

Manuscript received November 3, 2009
Manuscript accepted June 22, 2010
Manuscript handled by Darrell Henry